Available online at www.sciencedirect.com
ScienceDirect
International Journal of Heat and Mass Transfer 50 (2007) 4468–4487
International Journal of HEAT and MASS TRANSFER
www.elsevier.com/locate/ijhmt

# Transient modeling of heat, mass and momentum transfer of an evaporating cerium nitrate solution droplet with a surrounding shell in a rf thermal argon–oxygen plasma under reduced pressure

I. Castillo, R.J. Munz *

*Department of Chemical Engineering, McGill University, 3610 University St. Wong Building, Montreal, Quebec, Canada H3A 2B2*

Received 26 July 2006; received in revised form 27 March 2007
Available online 14 June 2007

**Abstract**

A model was developed to study the evaporation of a solution droplet surrounded by a porous crust in a stagnant rf Ar–$O_2$ thermal plasma under reduced pressure. This model considered a three phase system: a liquid core of dissolved $Ce(NO_3)_3 \cdot 6H_2O$ in water, a porous crust of homogeneously precipitated spherical crystals of equal size containing water vapor, and an Ar–$O_2$ plasma under reduced pressure. The model was solved considering a receding solution/crust interface in an ALE frame using temperature and composition dependant thermophysical properties. Darcy flow with a Knudsen correction to account for the gaseous flow through a porous media composed of nano-sized crystals was employed. The strength of the solid/liquid interface was calculated by computing the strength of liquid bridges formed at this interface. This value was compared to the pressure build-up caused by solvent evaporation and the point of crust breakage was determined at different operating conditions. The effects of plasma gas temperature, pressure and composition, droplet size, size of precipitated crystals and crust porosity on crust bursting were studied. The results showed that crust bursting occurred for all the conditions analyzed and that plasma temperature, droplet size and the size of the precipitated crystals had a significant effect on pressure build-up.


*Keywords:* Evaporation; Solution droplet; Crust formation; Cerium nitrate; Thermal plasma; ALE model; Darcy flow; Knudsen effect; Liquid bridges

## 1. Introduction

The manufacturing of ceramic powders from liquid precursors using radio frequency (rf) thermal plasmas has been developed in the past 10 years [1–5]. This technique consists of the evaporation and calcination of atomized solution droplets injected axially to the plasma core usually under reduced pressure. The solution is atomized by a liquid blast atomizer that provides a log-normal droplet size distribution centered around 20–30 μm in diameter. The droplets usually contain a non-volatile salt (nitrates, acetates, chlorides, etc.) dissolved in water or any other suitable solvent. The hot plasma environment provides the driving force for evaporation and calcination of the salt, resulting in the production of high-purity oxide particles. Thus, oxygen-rich plasmas are often employed. The use of liquid precursors encompasses applications such as production of ceramic materials for solid oxide fuel cells (SOFC) (perovskites, $Y_2O_3$, $CeO_2$, NiO, etc.) [6,7] and thermal barrier coatings ($ZrO_2$) [8]. It has been found in previous studies [7,9] that this technique can produce ceramic particles of known and controlled stochiometry. However these particles varied greatly in size from few nanometers to micron sizes, suggesting that more than one droplet-to-particle conversion mechanism was possible.

The production of ceramic powders in thermal plasmas from liquid precursors is similar to the well known spray pyrolysis technique [10], but the operating temperatures

* Corresponding author. Tel.: +1 514 398 4277; fax: +1 514 398 6678.
*E-mail address:* richard.munz@mcgill.ca (R.J. Munz).

0017-9310/$ - see front matter © 2007 Elsevier Ltd. All rights reserved.
doi:10.1016/j.ijheatmasstransfer.2007.05.001

**Nomenclature**

| | |
|---|---|
| $C$ | convective velocity (relative velocity between the material V and mesh velocity $\Psi$), [m/s] |
| $C_i$ | concentration of electrolyte $i$, [mol/L] |
| $C_p$ | heat capacity, [J/kg K] |
| $D_{12}$ | diffusion coefficient based on molecular concentration [$m^2$/s] |
| $F$ | Faraday constant |
| $F_{cs}$ | capillary and surface force, [N] |
| $h$ | enthalpy, [J/kg] |
| $K$ | crust permeability, [$m^2$] |
| $Kn$ | Knudsen number, $Kn = \lambda/2R_{sp}$ |
| $k$ | thermal conductivity, [W/m K] |
| $m$ | molality of the solute, [mol/kg solvent] |
| $\dot{m}$ | mass flow rate at the droplet surface due to vaporization, [kg/$m^2$ s] |
| $M$ | molecular weight, [kg/kg mol] |
| $M_{av}$ | average gas molecular weight, [kg/kg mol] |
| $P$ | pressure, [Pa] |
| $P_{max}$ | maximum droplet pressure, [Pa] |
| $P_{in}$ | droplet pressure, [Pa] |
| $P_{out}$ | pressure at the crust/gas interface, [Pa] |
| $P_i$ | partial pressure of $i$, [Pa] |
| $P^s$ | saturation pressure of water, [Pa] |
| $P_m$ | mean pressure difference across the crust, [Pa] |
| $Q$ | source/sink term, [J/$m^3$ s] |
| $r$ | radial distance, [m] |
| $R_{L(t)}$ | radius of the droplet (function of time), [m] |
| $R_C$ | inner crust radius, [m] |
| $R_g$ | universal gas constant, [J/kmol K] |
| $R_{sp}$ | radius of precipitated crystals in porous crust, [m] |
| $\dot{R}_L$ | change of droplet radius with respect to time, [m/s] |
| $T$ | temperature, [K] |
| $T_d$ | dimensionless temperature |
| $t$ | time, [s] |
| $t_{ch}$ | "thickness" of the liquid bridges, [m] |
| $T_r$ | reference temperature, [K] |
| $U$ | radial Darcian velocity, [m/s] |
| $V$ | radial material velocity, [m/s] |
| $V_m$ | molar volume of liquid phase, [$m^3$/mol] |
| $W_i$ | mass fraction of $i$ in liquid |
| $W_i^s$ | mass fraction of $i$ in liquid at saturation (constant over the range of temperature studied) |
| $x_i$ | mol fraction of $i$ in liquid |
| $Y_i$ | mass fraction of $i$ in gas |
| $z_i$ | mol fraction of $i$ in gas |

*Greek symbols*

| | |
|---|---|
| $\beta$ | half filled angle |
| $\varepsilon$ | porosity |
| $\gamma_\pm$ | mean ionic activity coefficient of the solute |
| $\lambda$ | mean free path, [m] |
| $\lambda_+^0$, $\lambda_-^0$ | limiting (zero concentration) ionic conductances, [(A/$cm^2$)(V/cm)(mol/$cm^3$)] |
| $\mu_C$ | gas viscosity in crust, [kg/m s] |
| $\mu_G$ | gas viscosity in gas phase, [kg/m s] |
| $\mu_l$ | water viscosity in the droplet, [kg/m s] |
| $\rho_L$ | density of liquid solution, [kg/$m^3$] |
| $\rho_C$ | density of gas in crust, [kg/$m^3$] |
| $\rho_G$ | density of gas in gas phase, [kg/$m^3$] |
| $\sigma_{LG}$ | surface tension, [N/m] |
| $\sigma_i$ | coefficient characteristic of each ion |
| $\sigma_y$ | crust yield stress, [N/$m^2$] |
| $\upsilon_+$, $\upsilon_-$ | valences of cation and anion, respectively |
| $\theta$ | wetting angle |
| $\Psi$ | mesh velocity, [m/s] |

*Subscripts*

| | |
|---|---|
| 1 | component 1 (either in the solution or the gas phase) |
| 2 | component 2 (either in the solution or the gas phase) |
| Ar | argon |
| d | dimensionless |
| C | crust domain |
| G | plasma gas domain |
| $i$ | $i$-component |
| $L$ | solution droplet domain |
| 0 | initial value |
| $O_2$ | oxygen |
| s | anhydrous salt |
| w | water |
| $\chi$ | referential domain or moving mesh |
| $\infty$ | conditions at infinity (far away from the droplet) |

*Superscript*

| | |
|---|---|
| s | saturated condition |

are higher, the droplets are often in the low micro size range (<50 μm) and the reactor chamber is operated under vacuum. As a result, the thermal plasma treatment is a more "rapid" version of spray pyrolysis, since the conditions for solvent evaporation are enhanced. Previous theoretical and experimental work, including our own studies [11], has shown that solution droplets containing non-volatile solutes tend to form a thin crust surrounding the evaporating droplet.

The crust is formed because the non-volatile salt precipitates out of solution, primarily at the droplet surface. A fast evaporation rate removes solvent from the droplet surface more quickly than it can be replenished by mass diffusion, resulting in the formation of a crust [12]. Having a

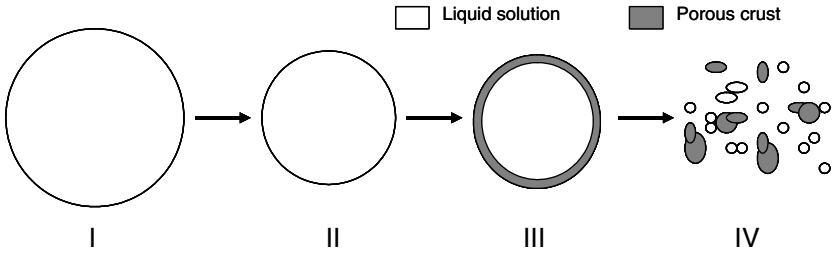


Fig. 1. Mechanism of droplet to particle conversion considering crust shattering.

crust around an evaporating liquid core retards the rate at which inner solvent escapes from the droplet [13], because the solvent must travel through a porous phase. This leads to an increase of the solvent vapor pressure that causes fracturing and/or bursting of the crust. As a consequence, after calcination takes place, solid particles of different sizes are formed (Fig. 1). A recent study by Ozturk [14] has shown that solid and hollow particles of $ZrO_2$ can be produced using thermal plasmas from zirconium acetate depending on the plasma operating conditions.

Even though pressure build-up inside the crust as a result of solvent evaporation is widely accepted as the main cause of crust bursting, few papers discuss this issue in detail [13,15]. The shattering of the crust is often related to the degree of superheating of the solution inside the crust and whether the liquid has reached its boiling point. This type of analysis provides little insight of the actual "forces" that prevent the crust from bursting. Therefore, an analysis of these forces acting at the receding crust/droplet interface will give a more realistic picture of when the crust will burst due to pressure build up.

Three different phases co-exist at the droplet/crust interface, i.e. a liquid solution wetting a solid crust and a gaseous evaporating solvent. The solution forms liquid bridges in the form of menisci that connect the newly precipitated solid particles along this interface. The forces present in these bridges are surface tension and a negative capillary pressure as a result of the solid particle curvatures. These two forces are commonly combined and termed capillary forces. The detailed description of meniscus properties and the capillary force for pendular liquid rings has been extensively investigated [16–18]. However, the connection of these forces to the problem of evaporating solution droplets with a surrounding crust has not been made to the authors' knowledge. Also, as a result of the small droplet size (20–30 μm in diameter), the precipitated particles forming the crust are likely to be in the nanometer range (i.e. the size of single precipitated crystals). Hence, the flow of evaporating solvent through porous media lies within the transient flow regime ($0.1 < Kn < 10$), between a continuum flow and a free molecular flow. This effect was considered in this work and it was adapted from the work of Tang [19].

In this paper, the effect of temperature, pressure, gas composition, crust porosity, size of precipitated crystals and initial droplet size (including crust and inner liquid core) were examined under thermal plasma conditions. The droplets contained a hexahydrated salt, $Ce(NO_3)_3 \cdot 6H_2O$, dissolved in water, surrounded by a porous crust containing water vapor. The mass and thermal histories inside the droplet and throughout the crust were studied. The droplet/crust interface was allowed to recede in time as water was continuously being evaporated. Darcy flow with a Knudsen correction was used for the crust section.

The purpose of this study is to derive understanding of how plasma conditions affect droplet and crust mass and thermal histories and to predict the onset of crust shattering under typical rf thermal plasma operating conditions.

## 2. Model development

The physical model studied was the transient evaporation of a solution droplet approximately 30 μm in diameter surrounded by a porous crust (Fig. 2). The droplet and its crust are immersed in a mixture of stagnant argon–oxygen rf plasma. The solution droplet was a hexahydrated salt, $Ce(NO_3)_3 \cdot 6H_2O$, dissolved in water and all water of hydration is assumed to be released and to be part of the total droplet water content. The anhydrous salt was consid-

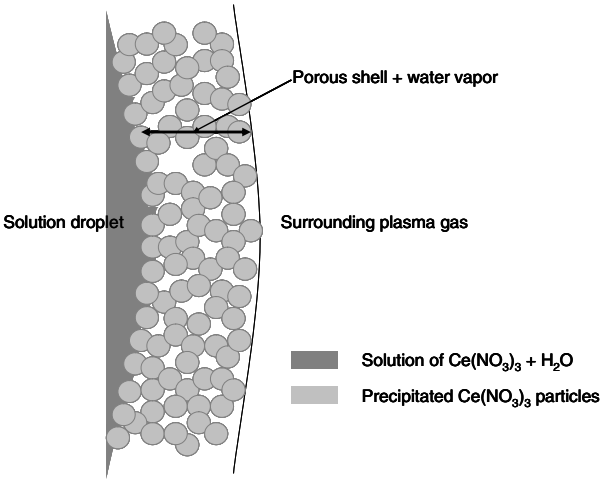


Fig. 2. Cross section of an evaporating droplet showing the inner liquid core, the homogeneously precipitated spherical crystals particles of a given size comprising the crust and the surrounding plasma gas.

ered to remain largely in molecular form (i.e. as $Ce(NO_3)_3$) as a result of a large salt content in the droplet but whenever possible solution properties were calculated assuming dissociation of the nitrate and the cerium ions. The droplet has reached the point of saturation at the droplet/crust interface.

The porous crust is assumed to be rigid and in the shape of a spherical shell with a receding droplet/crust interface. Water vapor is formed at the liquid/crust interface and it then escapes through the porous shell, which is composed of homogeneously nucleated spherical crystals a few nanometers in diameter. These nucleated crystals are assumed to be of uniform size and provide the crust with a characteristic porosity. This porosity is maintained across the whole thickness of the crust. Capillary and surface tension forces prevent crust from bursting through the formation of liquid bridges between the spherical crystals.

Radiation and second order effects, such as Soret and Dufor effects, were assumed to be negligible. Spherical symmetry reduced the problem to a transient, three phase process of one dimensional nature. The only fluid motion present was a radial flow field through the crust and into the gas phase induced by water vaporization. Darcy flow is assumed in the crust with a non-continuum correction factor as the Knudsen number falls within the transition regime ($0.1 < Kn < 10$). Radial flow inside the droplet was neglected on the basis of the large density difference between the solution droplet and the gas. Viscous dissipation effects were neglected. Finally, the surrounding plasma gas (argon/oxygen) obeyed the ideal gas law.

Under these conditions the physics of the problem are as follows: solvent (i.e. water) evaporates from the solution droplet which causes droplet shrinkage and crust growth. The salt diffuses toward the centre of the droplet and a temperature profile is developed in the droplet. The water vapor escapes through the porous crust and mixes with the surrounding plasma gas. A temperature profile also develops in the crust. The crust opposes solvent flow and allows heat transfer from the surrounding gas into the droplet. This process continues while pressure builds up at the droplet/crust interface as a result of increasing temperature and crust obstruction to flow. This increasing pressure exerts a stress along the droplet/crust interface that is counterbalanced by capillary and surface forces. When this stress exceeds the magnitude of the counterbalancing forces, the crust bursts.

It is then hypothesized that the resulting fragments, i.e. smaller droplets and crust pieces undergo thermolysis and the $Ce(NO_3)_3$ salt is transformed into $CeO_2$ particles. Consequently a multi-modal particle size distribution is expected (Fig. 1, IV).

This model was solved using the Arbitrary-Lagrangian–Eulerian (ALE) method which has been successfully employed with moving boundary problems [20]. A deformed mesh can be used when the boundaries of the computational domain deform in time as a result of the physics of the problem, in this case, the evaporation of the solution droplet. Therefore, a new mesh is not needed at each time step; instead the mesh nodes are perturbed so that they conform to the moving boundaries [21]. In this way, computational time can be saved without losing resolution in the solution.

### 2.1. Liquid governing equations

For the liquid phase, $r < R_L(t)$, (1) refers to the water and (2) refers to the anhydrous salt (i.e. $Ce(NO_3)_3$) species equation

$$\frac{\partial}{\partial t}(r^2\rho_L W_1)\bigg|_\chi + \frac{\partial}{\partial r}\left(-r^2\rho_L D_L \frac{\partial W_1}{\partial r}\right) = 0 \tag{1}$$

energy equation including Steffan diffusion in the ($h_1 - h_2$ term)

$$\frac{\partial}{\partial t}(r^2\rho_L C_{p_L} T)\bigg|_\chi + \frac{\partial}{\partial r}\left(-r^2 k_L \frac{\partial T}{\partial r} - r^2\rho_L D_L \frac{\partial W_1}{\partial r}(h_1 - h_2)\right) = 0 \tag{2}$$

### 2.2. Shell governing equations

For the porous crust, $R_{L(t)} < r < R_C$, (1) refers to the water and (2) refers to the plasma gas argon–oxygen mixture. The convective velocity is defined as $C = V - \psi$.
Species equation

$$\frac{\partial}{\partial t}(r^2\varepsilon\rho_C Y_1)\bigg|_\chi + \frac{\partial}{\partial r}\left(-r^2\rho_C D_C \frac{\partial Y_1}{\partial r} + r^2\rho_C Y_1 C\right) = 0 \tag{3}$$

energy equation including Steffan diffusion in the ($h_1 - h_2$ term)

$$\frac{\partial}{\partial t}(r^2\rho_C C_{p_C} T)\bigg|_\chi + \frac{\partial}{\partial r}\left(-r^2 k_C \frac{\partial T}{\partial r} - r^2\rho_C D_C \frac{\partial Y_1}{\partial r}(h_1 - h_2) + r^2\rho_C C_{p_C} TC\right) = 0 \tag{4}$$

Darcy equation

$$U = -\frac{K}{\mu_C}\frac{\partial P}{\partial r} \tag{5}$$

Darcian velocity $U$ is related to $V$ by $U = \varepsilon V$
Continuity equation

$$\frac{\partial}{\partial t}(r^2\varepsilon\rho_C)\bigg|_\chi + \frac{\partial}{\partial r}(r^2\rho_C U) = 0 \tag{6}$$

which can be also expressed as (combining Eqs. (5) and (6))

$$\frac{\partial}{\partial t}(r^2\varepsilon\rho_C)\bigg|_\chi + \frac{\partial}{\partial r}\left(r^2\rho_C\left(-\frac{K}{\mu_C}\frac{\partial P}{\partial r}\right)\right) = 0 \tag{7}$$

Table 1
Thermophysical properties

| Property | Method | Mixing rule |
|---|---|---|
| *Liquid properties* | | |
| Density [kg/m$^3$] | Ideal mixing | $\rho_L = aW_1 + bW_2$; $a = 1000, b = 1600$[a] |
| Specific heat [J/kg$^{-1}$ K$^{-1}$] | Ideal mixing | $C_{p_1} = a + bT + cT^2 + dT^3$, $a = 8.958 \times 10^3$, $b = -4.053 \times 10^1$, $c = 1.124 \times 10^{-1}$, $d = -1.014 \times 10^{-4}$ [26]<br>$C_{p_2} = 358.06$ [27]<br>$C_{p_L} = C_{p_1} W_1 + C_{p_2} W_2$ |
| Thermal conductivity [W/m K] | Riedel for aqueous solutions [27] | $k_{1(T_r)} = a + bT + cT^2$; $a = -3.838 \times 10^{-1}$, $b = 5.254 \times 10^{-3}$, $c = -6.369 \times 10^{-6}$<br>$k_{L(T_r)} = k_{1(T_r)} + \Sigma \sigma_i C_i$; $\sigma(NO_3^-) = -6.978 \times 10^{-5} \sigma(Ce^{4+}) = -43.61 \times 10^{-5}$<br>$k_{L(T)} = k_{L(T_r)} * k_{1(T)}/k_{1(T_r)}$ |
| Binary diffusion coefficient [m$^2$/s] | Nerst–Haskell equation and Gordon approach for concentrated solutions [27] | $D^o_{12} = R_g T/F^2 * (1/\upsilon_+ + 1/\upsilon_-)/(1/\lambda^0_+ + 1/\lambda^0_-)/1 \times 10^4$;<br>$D_{12(T_r)} = D^o_{12}(\eta_s/\eta)(\rho_s V_s) * (1 + m\partial \ln \gamma_\pm/\partial m)$[c]<br>$D_{12(T)} = D_{12(T_r)}(T/T_r)\mu_{1(T_r)}/\mu_{1(T)}$<br>$\partial \ln \gamma_\pm/\partial m$ [29][b] |
| Water viscosity [kg/m s] | | $M_1 = a + bT + cT^2 + dT^3$; $a = -2.471 \times 10^1$, $b = 4.209 \times 10^3$, $c = 4.527 \times 10^{-2}$, $d = -3.376 \times 10^{-5}$ [28] |
| Enthalpy of water [J/kg] | | $h_1 = a + bT + cT^2 + dT^3$; $a = -2.248 \times 10^6$, $b = 1.297 \times 10^4$, $c = -2.291 \times 10^1$, $d = 1.962 \times 10^{-2}$ |
| Enthalpy of $Ce(NO_3)_3$ salt [J/kg] | | $H_2 = h^o_2 + C_{p_2}(T - T_r)$ |
| *Gas properties* | | |
| Density [kg m$^{-3}$] | Ideal gas | $\rho_G = PM_{av}/R_g T$ |
| Specific heat [J kg$^{-1}$ K$^{-1}$] | Ideal mixing | $C_{p_1} = a + bT + cT^2 + dT^3 + eT^4$, $a = 1.652 \times 10^3$, $b = 1.295 \times 10^{-1}$, $c = 1.850 \times 10^{-3}$, $d = -1.959 \times 10^{-6}$, $e = 6.384 \times 10^{-10}$ [30]<br>$C_{p_{ox}} = a + bT + cT^2 + dT^3$, $a = 8.958 \times 10^3$, $b = -4.053 \times 10^1$, $c = 1.124 \times 10^{-1}$, $d = -1.014 \times 10^{-4}$<br>$C_{p_{ar}} = 520.4$ [31]<br>$C_{p_2} = Y_{Ar} M_{Ar} + Y_{O_2} M_{O_2}$<br>$C_{p_G} = C_{p_1} Y_1 + C_{p_2} M_2$ |
| Thermal conductivity [W m$^{-1}$ K$^{-1}$] | Wassiljewa equation with the Mason and Saxena modification [27] | $k_1 = a + bT + cT^2 + dT^3 + eT^4 + fT^5$; $a = -1.134 \times 10^{-2}$, $b = 2.402 \times 10^{-4}$, $c = -6.519 \times 10^{-7}$, $d = 9.231 \times 10^{-10}$, $e = -5.506 \times 10^{-13}$, $f = 9.944 \times 10^{-17}$,<br>$k_{ar} = a + bT$; $a = 1.944 \times 10^{-2}$, $b = 2.464 \times 10^{-5}$,<br>$k_{ox} = a + bT + cT^2 + dT^3$; $a = -1.197 \times 10^{-2}$, $b = 1.342 \times 10^{-4}$, $c = -6.456 \times 10^{-8}$, $d = 1.782 \times 10^{-11}$<br>$k_G = z_1 k_1/(z_1 + z_2 \Phi_{12}) + z_2 k_2/(z_2 + z_1 \Phi_{21})$[e] |
| Viscosity [kg m$^{-1}$ s$^{-1}$] | Wassiljewa equation with the Mason and Saxena modification [27] | $M_1 = a + bT + cT^2 + dT^3$; $a = -5.424 \times 10^{-6}$, $b = 4.855 \times 10^{-8}$, $c = -5.722 \times 10^{-12}$, $d = -2.946 \times 10^{-16}$<br>$\mu_{ar} = a + bT$; $a = 2.975 \times 10^{-5}$, $b = 2.893 \times 10^{-8}$<br>$\mu_{ox} = a + bT$; $a = 2.326 \times 10^{-5}$, $b = 2.799 \times 10^{-8}$<br>$\mu_G = z_1 \mu_1/(z_1 + z_2 \Phi_{12}) + z_2 \mu_2/(z_2 + z_1 \Phi_{21})$,<br>$\Phi_{12} = [1 + (\mu_1/\mu_1)^{1/2} (M_2/M_1)^{1/4}]^2/[8(1 + (M_1/M_2))]^{1/2}$,<br>$\Phi_{21} = \Phi_{12}(\mu_2/\mu_1)(M_1/M_2)$[d] |
| Binary diffusion coefficient [m$^2$ s$^{-1}$] | Lennard–Jones [32] | $D_{12} = 1.8585 \times 10^{-7} * \sqrt{(T^3(1/M_1 + 1/M_2))} * 1/(P\sigma^2_{12}\Omega_{12})$[f] |
| Enthalpy of water [J/kg] | | $h_1 = a + bT + cT^2 + dT^3 + eT^4$; $a = 3.443 \times 10^6$, $b = -4.374 \times 10^3$, $c = 8.618, d = -4.515 \times 10^{-2}$, $e = 8.496 \times 10^{-7}$ |
| Enthalpy of plasma gas [J/kg] | | $h_{ar} = a + bT$; $a = -1.551 \times 10^{-1}$, $b = 5.203 \times 10^{-4}$,<br>$h_{ox} = a + bT + cT^2$; $a = -2.849 \times 10^{-1}$, $b = 9.213 \times 10^{-4}$, $c = 7.478 \times 10^{-8}$,<br>$h_2 = h_{Ar} Y_{Ar} + h_{O_2} Y_{O_2}$, |
| Molecular weights [kg/kgmol] | | $M_2 = z_{Ar} M_{Ar} + z_{O_2} M_{O_2}$; $M_{av} = z_1 M_1 + z_2 M_2$ |
| *Crust properties* | | |
| Density [kg m$^{-3}$] | Ideal gas | $\rho_C = PM_{av}/R_g T$ |
| Specific heat [J kg$^{-1}$ K$^{-1}$] | Ideal mixing | $C_{p_G} = C_{p_1} Y_1 + C_{p_2} M_2$ (calculated as in the gas phase); $C_{p_s} = a + bT$; $a = 364.3, b = 0.061$[g] [33]<br>$C_{p_C} = C_{p_G} * \varepsilon + C_{p_s} * (1 - \varepsilon)$ |
| Thermal conductivity [W m$^{-1}$ K$^{-1}$] | Kaviany [34] | $k_G = z_1 k_1/(z_1 + z_2 \Phi_{12}) + z_2 k_2/(z_2 + z_1 \Phi_{21})$ (calculated as in the gas phase); $k_s = 0.5$ W/m K[h]<br>$k_C = k_G * (k_s/k_G)\text{^}(0.280 - 0.757 * \log(\varepsilon) - 0.057P * \log(k_s/k_G))$ |
| Viscosity [kg m$^{-1}$ s$^{-1}$] | | $\mu_G = \mu_C$ (calculated as in the gas phase) |

Table 1 (*continued*)

| Property | Method | Mixing rule |
|---|---|---|
| Binary diffusion coefficient [$m^2\ s^{-1}$] | Kaviany [34] | $D_{12G} = D_{12C}$ (calculated as in the gas phase)<br>$D_C = D_{12C} * 2 * \varepsilon * (1 - Y_i)/(3 - \varepsilon)$ |
| Permeability [$m^2$] | Tang et al. [19] | $\lambda = (\mu_C * \pi * R_g * T/2 * P_m * M_{av})^{0.5}$; $Kn = \lambda/2 * R_{sp}$;<br>$K = R_{sp}^2 * (1 + 8 * C_1 * Kn + 16 * C_2 * Kn^2)/8; C_1 = 1.1466, C_2 = 0.14$ |
| Enthalpy of water [J/kg] | | $h_{1G} = h_{1C}$ (calculated as in the gas phase) |
| Enthalpy of plasma gas [J/kg] | | $h_{2G} = h_{2C}$ (calculated as in the gas phase) |
| Molecular weights [kg/kg mol] | | $M_2 = z_{ar}M_{ar} + z_{ox}M_{ox}$; $M_{av} = z_1M_1 + z_2M_2$ |
| Enthalpy of vaporization [J/kg] | | $h_{1C} - h_{1L}$ |

For the liquid, the subindex 1 refers to water and 2 to the anhydrous salt. For the gas and crust, 1 refers to water vapor and 2 for the mixture of argon and oxygen plasma gas.

[a] Experimental values.

[b] The values of $Ce^{4+}$ were approximated from curve fitting values of $Gd^{3+}$ and $Sm^{3+}$.

[c] The product of these ratios are $(\eta_s/\eta)(\rho_s V_s) \sim 1$.

[d] To obtain $\mu_2$ the same mixing rule was applied but 1 and 2 are argon and oxygen, respectively.

[e] The same formulae are used to calculate $\Phi_{12}$ and $\Phi_{21}$ for the thermal conductivity as for viscosity.

[f] Since argon and oxygen had similar Lennard–Jones potentials, only the values of oxygen are considered which allows the calculation of multicomponent diffusion coefficients. Only, in this case 2 refers to oxygen.

[g] The heat capacity of $CeO_2$ is assumed to be the heat capacity of the solid part composing the porous crust.

[h] The thermal conductivity of $CeO_2$–$ZrO_2$ plasma sprayed layers (University of Sherbrooke personal communication) was used as the thermal conductivity of the porous layer.

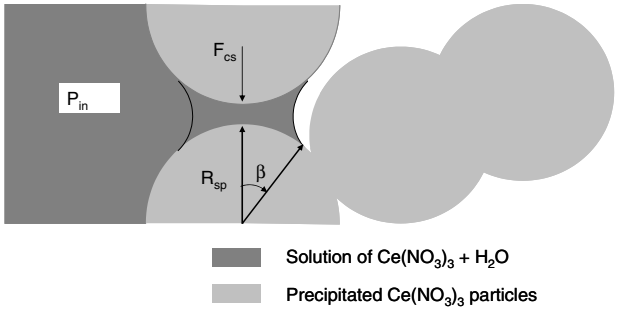


Fig. 3. Sketch showing the liquid bridges and the forces present. The bridges are formed between precipitated spherical crystals at the liquid crust interface.

### 2.3. Gas governing equations

For the gas phase, $r > R_C$, (1) refers to the water and (2) refers to the plasma gas argon–oxygen mixture.

Continuity equation

$$r^2\frac{\partial \rho_G}{\partial t} + \rho_G\left(r^2\frac{\partial V}{\partial r} + 2rV\right) + r^2V\frac{\partial \rho_G}{\partial r} = 0 \tag{8}$$

Species equation

$$\frac{\partial}{\partial t}(r^2\rho_G Y_1) + \frac{\partial}{\partial r}\left(-r^2\rho_G D_G\frac{\partial Y_1}{\partial r} + r^2\rho_G Y_1 V\right) = 0 \tag{9}$$

Energy equation

$$\frac{\partial}{\partial t}(r^2\rho_G C_{p_G} T) + \frac{\partial}{\partial r}\left(-r^2 k_G\frac{\partial T}{\partial r} - r^2\rho_G D_G\frac{\partial Y_1}{\partial r}(h_1 - h_2) + r^2\rho_G C_{p_G} TV\right) = Q$$

$$Q = -r^2 P\left(\frac{\partial V}{\partial r}\right) \tag{10}$$

Momentum equation

$$\frac{\partial}{\partial t}(r^2\rho_G V) = \frac{\partial}{\partial r}\left(r^2\left[2\mu\frac{\partial V}{\partial r} - P\right]\right) + r^2\left(F - \rho V\frac{\partial V}{\partial r} - \frac{2(2\mu V/r - P)}{r}\right)$$

$$F = -\frac{\partial}{\partial r}\left(\frac{2}{3}\mu\left(\frac{\partial V}{\partial r}\right)\right) \tag{11}$$

### 2.4. Boundary conditions

At droplet center

$$\frac{\partial W_i}{\partial r} = \frac{\partial T}{\partial r} = 0 \tag{12}$$

At liquid/crust interface

$$W_i = W_{si} \tag{13}$$

Table 2
Summary of simulation parameters

| No. | Plasma temperature ($T_\infty$) [K] | Initial droplet size diameter [μm] | Gas pressure ($P_\infty$) [atm] | Shell porosity ($\varepsilon$) | Radius of precipitated crystals ($R_{sp}$) [nm] | Plasma gas composition ($Ar/O_2$) mol fraction ($Z_{Ar}/Z_{O2}$) |
|---|---|---|---|---|---|---|
| 1 | 600 | 30 | **0.3** | 0.4 | 10 | 0.2/0.8 |
| 2 | **700** | **40** | 0.4 | **0.5** | **20** | **0.3/0.7** |
| 3 | 800 | 50 | 0.5 | 0.6 | 30 | 0.4/0.6 |

Overall mass

$$\dot{m} = \rho_C(V - \dot{R}_L)_C = \rho_L\left(0 - \dot{R}_L\right)_L \tag{14}$$

Species balance

$$(n_{iC} - \dot{R}_L \rho_C)_C = (n_{iL} - \dot{R}_L \rho_L)_L$$
$$n_{iC} = -\rho_C D_C \frac{\partial Y_i}{\partial r} + \rho_C Y_i C;\ n_{iL} = -\rho_L D_L \frac{\partial W_i}{\partial r} \tag{15}$$

Energy balance

$$e_L = -k_L \frac{\partial T}{\partial r} - \rho_L D_L \frac{\partial W_1}{\partial r}(h_1 - h_2)$$
$$e_C = -k_C \frac{\partial T}{\partial r} - \rho_C D_C \frac{\partial Y_1}{\partial r}(h_1 - h_2) + \rho_C C_{p_C} TV$$
$$\left(e_C - \dot{R}_L \sum_{i=1}^{n} \rho_C Y_i h_{iC}\right)_C = \left(e_L - \dot{R}_L \sum_{i=1}^{n} \rho_L W_i h_{iL}\right)_L \tag{16}$$

Kelvin's equation

$$\ln\left(\frac{P_i}{P^s}\right) = -\left(\frac{2\sigma_{LG}\cos\theta}{R_{sp}}\right)\left(\frac{V_m}{R_g T}\right);\quad P_i = Y_i \rho_C \frac{RT}{M_i} \tag{17}$$

At crust/gas interface

$$Y_i|_C = Y_i|_L;\ T|_C = T|_L;\ V|_C = V|_L;\ P|_C = P_i|_L \tag{18}$$

At infinity $r \to \infty$

$$Y_i = 0;\quad T = T_\infty;\quad V = 0;\quad \frac{\partial P}{\partial r} = 0 \tag{19}$$

### 2.5. Initial conditions

Overall mass conservation

$$-\rho_L \dot{R}_L|_{R_L} = \dot{m} + \int_0^{R(t)} \left(\frac{r}{R_L}\right)^2 \frac{\partial \rho_L}{\partial t}\, dr \tag{20}$$

In the liquid phase

$$W_i = W_{io};\ T = T_{Lo} \tag{21}$$

In the porous phase

$$Y_i = 0,\ T = T_{Lo},\ V = 0,\ P = Po \tag{22}$$

In the gas phase

$$Y_i = 0,\ T = T_{Go},\ V = 0,\ P = Po \tag{23}$$

### 2.6. Thermophysical properties

A more accurate formulation of the problem can be derived taking into account temperature and concentration dependence of the species in the liquid, crust and gas domains (Table 1).

### 2.7. Maximum pressure at droplet core

The maximum pressure that the evaporating solvent can exert on the crust before the crust shatters is given by the following equation [22]

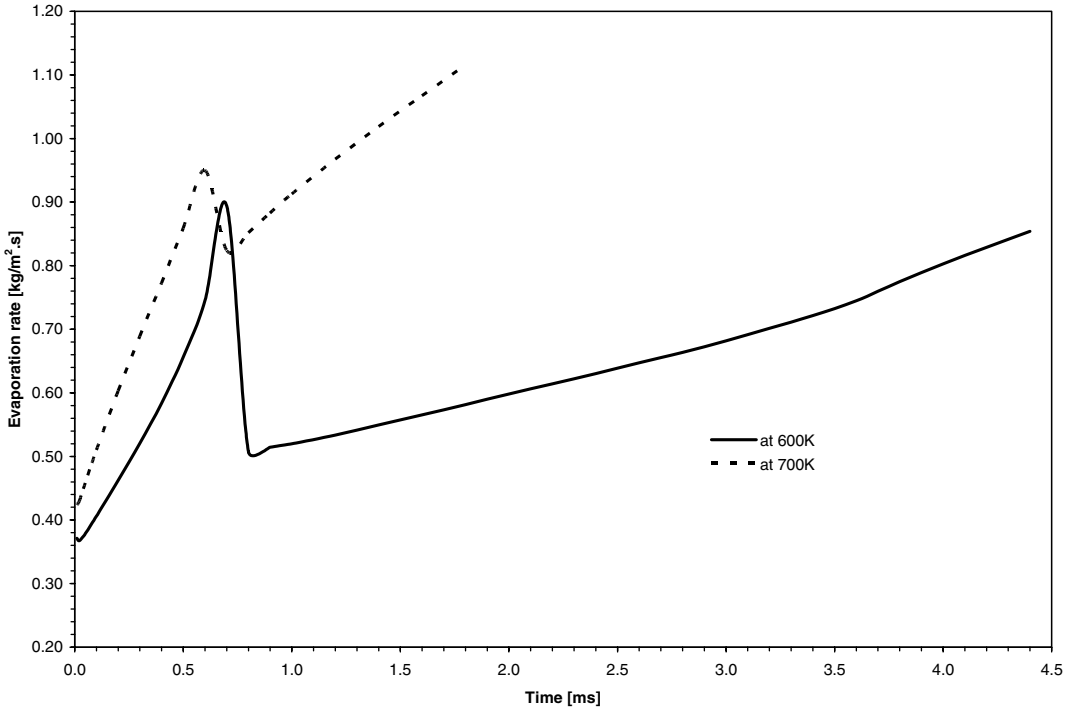


Fig. 4. Evaporation rate of the solution droplet before and after crust formation at two different plasma gas temperatures ($P = 0.3$ atm for 40 μm diameter droplets, $Z_{Ar} = 0.3/Z_{O_2} = 0.7$, $\varepsilon = 0.5$, $R_{sp} = 20$ nm).

$$\Delta P = P_{\max} - P_{\text{out}} = \frac{2^* \sigma^* t_{\text{ch}}}{R_{\text{L(t)}}} \tag{24}$$

This equation treats the evaporating droplet as if the core was a pressurized liquid kept within a rigid spherical shell of radius equal to the radius of the droplet; similar to a pressurized spherical vessel of a given "wall thickness" (Fig. 3).

The $\Delta P$ is the difference between the inner core pressure and the pressure at the crust/gas interface. The liquid bridges formed between the precipitated particles at the droplet/crust interface act as a "wall" of thickness equal

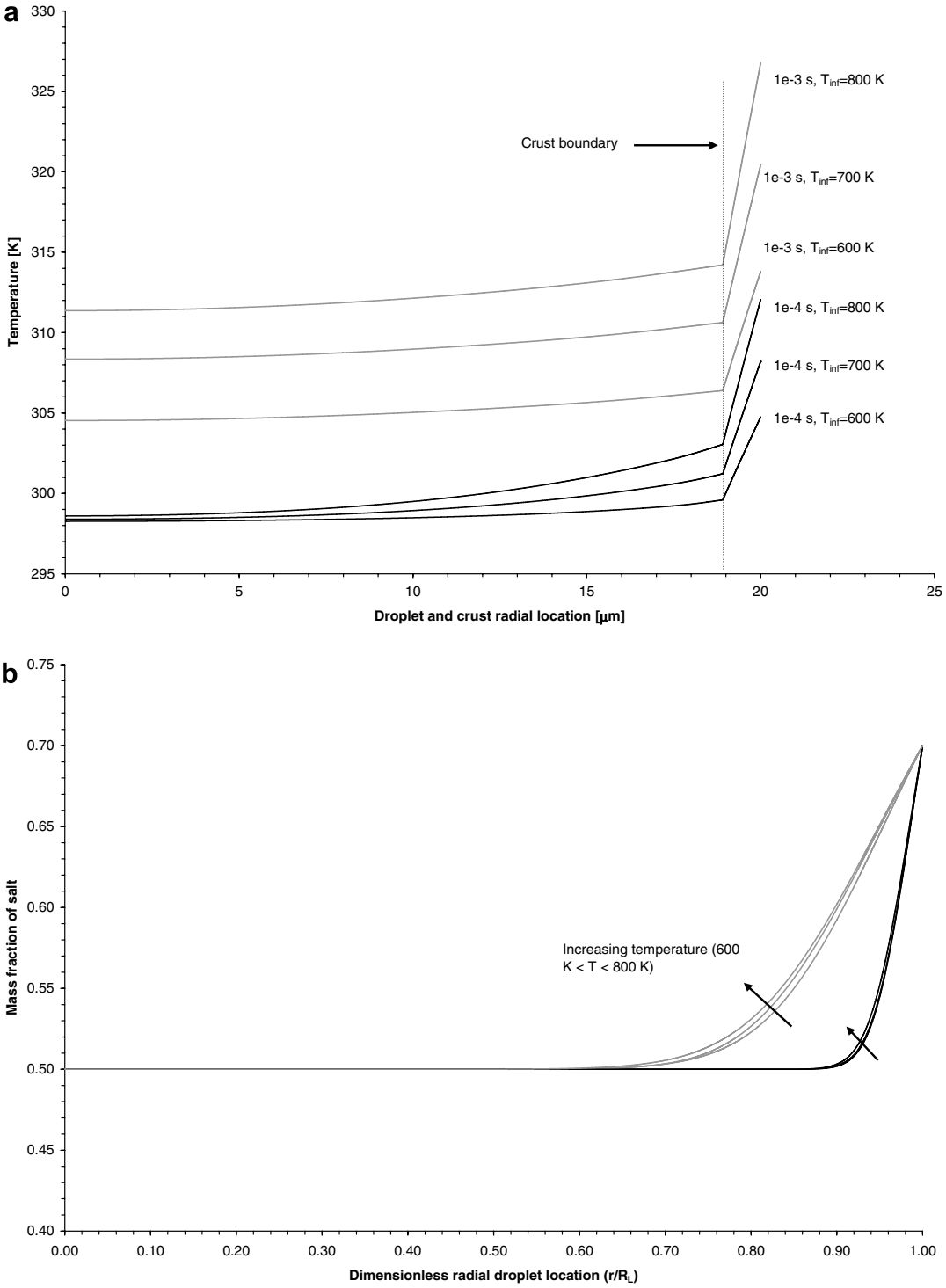


Fig. 5. Temperature profile in the droplet and crust (a) and mass fraction profile in the droplet (b) as a function of radial distance and temperature at $1 \times 10^{-4}$ and $1 \times 10^{-3}$ s ($P = 0.3$ atm for 40 μm diameter droplets, $Z_{\text{Ar}} = 0.3/Z_{\text{O}_2} = 0.7$, $\varepsilon = 0.5$, $R_{\text{sp}} = 20$ nm).

to $t_{ch} = 2R_{sp}\sin(\beta)$. This fictitious wall has a maximum yield stress ($\sigma_y$) that is equal to the ratio of the both the capillary and surface forces ($F_{ch}$) to the projected area over which these forces act on, as follows:

$$\sigma_y = \frac{F_{ch}}{\pi(R_{sp}\sin(\beta))^2} \tag{25}$$

The combined effect of capillary and surface forces was estimated using the method described by Willet [23], who calculated these forces for two spherical bodies connected by liquid bridges. It was assumed that the crust will burst when the pressure within the droplet exceeded this maximum pressure, i.e. when $P_{in}$ (calculated from the model) $= P_{max}$.

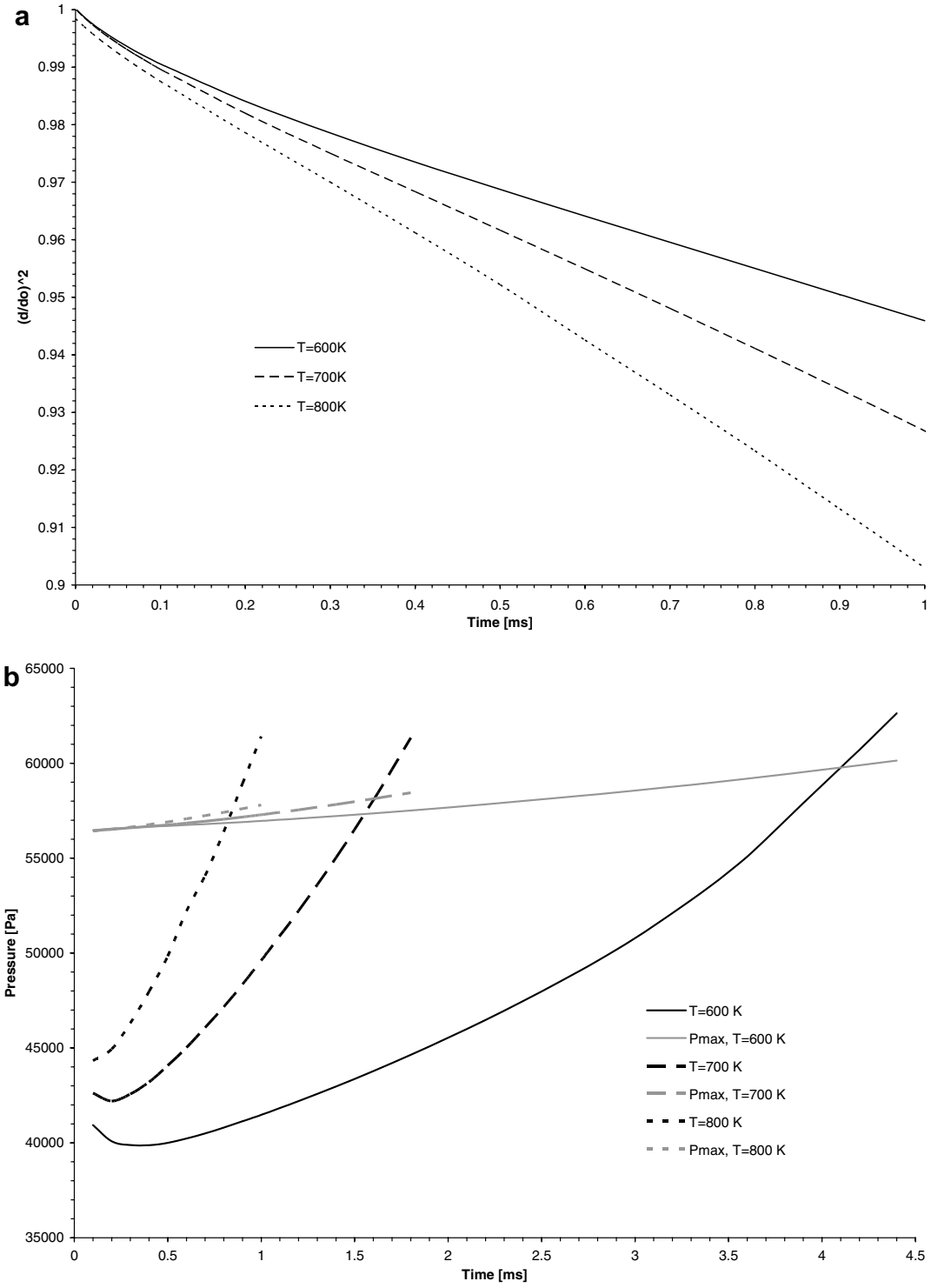


Fig. 6. Evolution of droplet diameter (a) and pressure build-up (b) as a function of time for different plasma temperatures ($P = 0.3$ atm for 40 μm diameter droplets, $Z_{Ar} = 0.3/Z_{O_2} = 0.7$, $\varepsilon = 0.5$, $R_{sp} = 20$ nm).

### 2.8. Solution procedure

Comsol Multiphysics® was used to solve the model. The model consisted of approximately 40,000 elements distributed in a non-uniform mesh, a higher number of elements were located at the droplet/crust interface and crust/gas interface. Mesh independent solutions were obtained. Quadratic Lagrange elements were used for all variables, except pressure in which linear elements were employed. Lagrange multipliers were used to improve solution convergence of the boundary conditions. A Heaviside step function [24] was applied to provide smooth temperature and

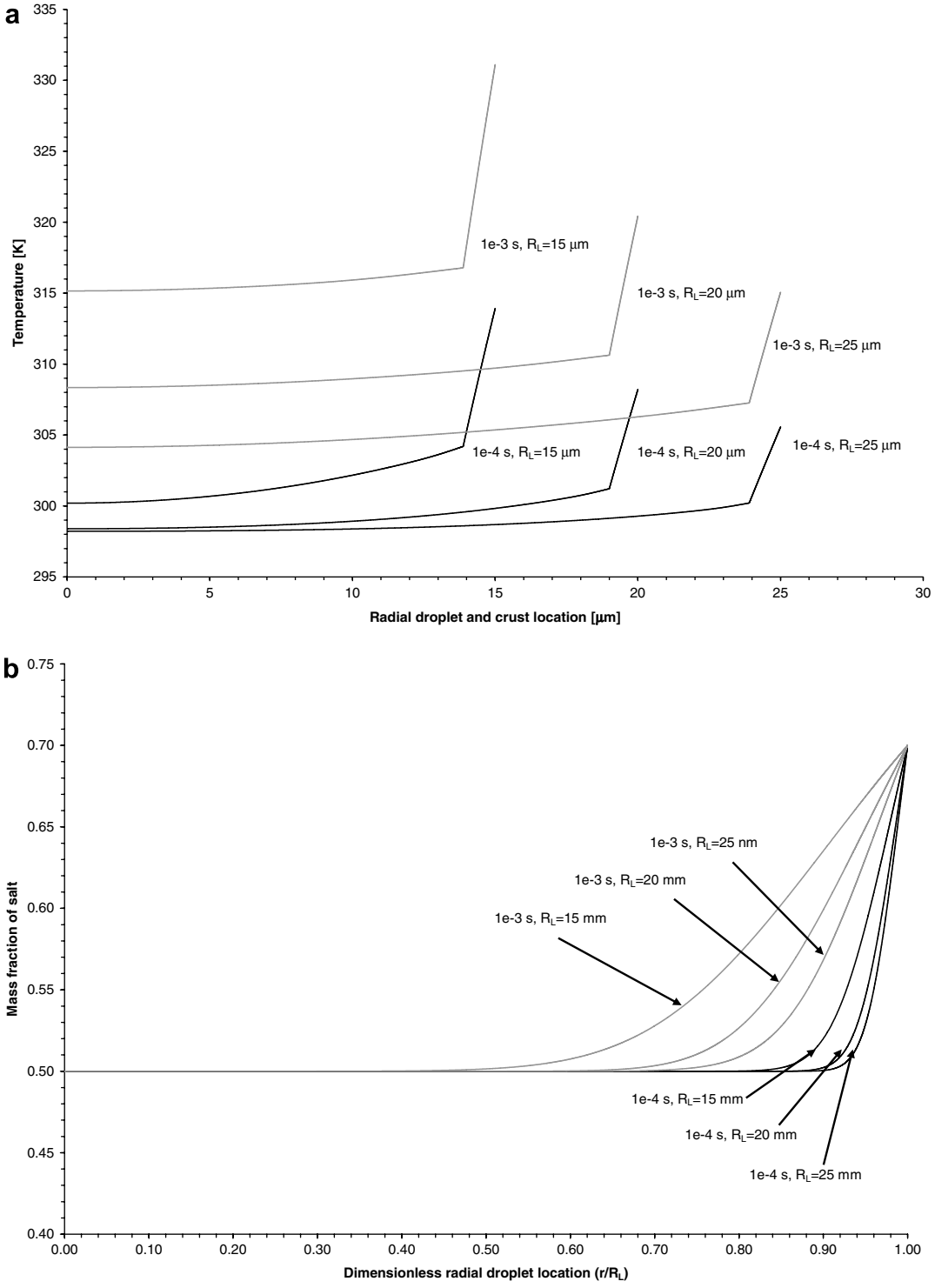


Fig. 7. Temperature profile in the droplet and crust (a) and mass fraction profile in the droplet (b) as a function of radial distance and initial droplet size at $1 \times 10^{-4}$ and $1 \times 10^{-3}$ s ($P = 0.3$ atm, $T_\infty = 700$ K, $Z_{Ar} = 0.3/Z_{O_2} = 0.7$, $\varepsilon = 0.5$ and $R_{sp} = 20$ nm).

concentration profiles as initial conditions in the vicinity of the droplet/crust interface and crust/gas interface. Heat and mass transfer equations were solved first, assuming a zero velocity flow. This provided a better initial solution estimate for the coupled heat-mass–momentum system at time zero ($t = 0$).

## 3. Model validation

This model was qualitatively validated by comparing the results obtained to the spray drying of droplets forming precipitated shells. The models available for spray drying often consider lower gas temperatures and are operated at atmospheric pressure. Few of these models even consider the drying of solution droplets surrounded by a porous crust due to the complexity of solving a three phase problem. To the authors' knowledge, the Knudsen effect has not previously been incorporated so a direct comparison to the available literature models cannot be made. However, a receding interface model of the drying of single drops of slurries of sodium sulfate decahydrate described by Cheong [25] showed remarkably similar features to our present work. These features involved the precipitation of a solute and crust formation and the subsequent simultaneous solution of heat, mass and momentum balance of the evaporating droplet. In Cheong's work, it was indicated that the rate of evaporation of a solution droplet *before* forming a crust increases with time. When the crust is formed, the evaporation rate sharply decreases but then this rate slowly increases again with time as more solvent is vaporized.

Hence to validate the model in this work, the results obtained in previous work [11] were used up to the point of crust formation, and then the present model was used from that point onwards. The results are plotted in Fig. 4 for two different plasma gas temperatures.

It can be seen that the evaporation rate sharply decreases when the crust is formed since the crust prevents the free flow of evaporating solvent. This rate then increases over time as a result of the higher thermal conductivity of the crust which increases the heat transferred to the inner core of the droplet. The trend showed in Fig. 4 is in agreement with what has been reported previously in the work by Cheong, thus providing some re-assurance that the model in this work can adequately portray the physics of solution droplets surrounded by a porous shell.

## 4. Results and discussion

The present model considers the effect of plasma temperature, initial droplet size, surrounding pressure, shell porosity, size of precipitated crystals and plasma gas composition. The solution droplet has reached the point of saturation at the droplet/solid interface (i.e. $\sim W_s = 0.7$). The porous crust was initially considered to be 0.1 μm thick. The crust is formed of homogeneously nucleated spherical crystals a few nanometers in diameter and water vapor. The initial crust thickness was assumed to be 0.1 μm which

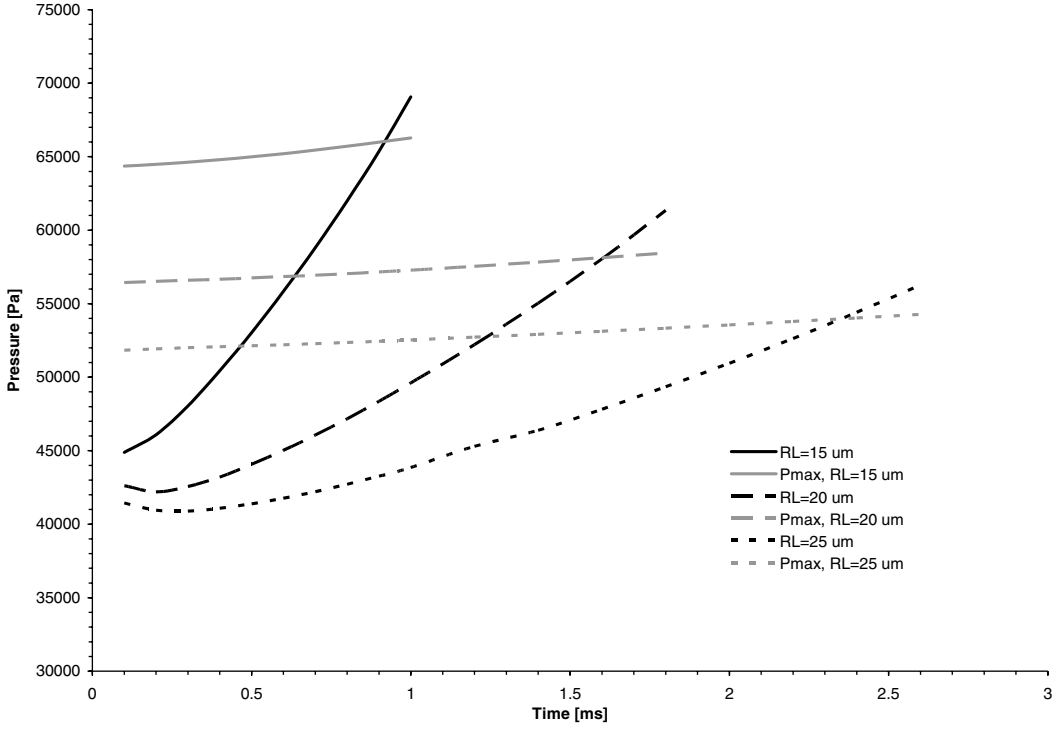


Fig. 8. Evolution of pressure build-up as a function of time for different initial droplet diameters ($P = 0.3$, $T_\infty = 700$ K, $Z_{Ar} = 0.3/Z_{O_2} = 0.7$, $\varepsilon = 0.5$ and $R_{sp} = 20$ nm).

is approximately between 2 and 3 times the diameter of 3 spherical crystals. This was considered to be the minimum crust thickness based on its minimum number of particles to form liquid bridges. Further solute precipitation was assumed to form similar spherical crystals too. The simulation was stopped when the pressure at this interface exceeded the maximum pressure resisted by the porous shell.

A summary of the different conditions investigated in this work is presented in Table 2. The base case conditions are in bold.

### 4.1. Effect of plasma temperature

The surrounding plasma temperature was increased from 600 K to 800 K ($T_\infty$). The temperature profiles in

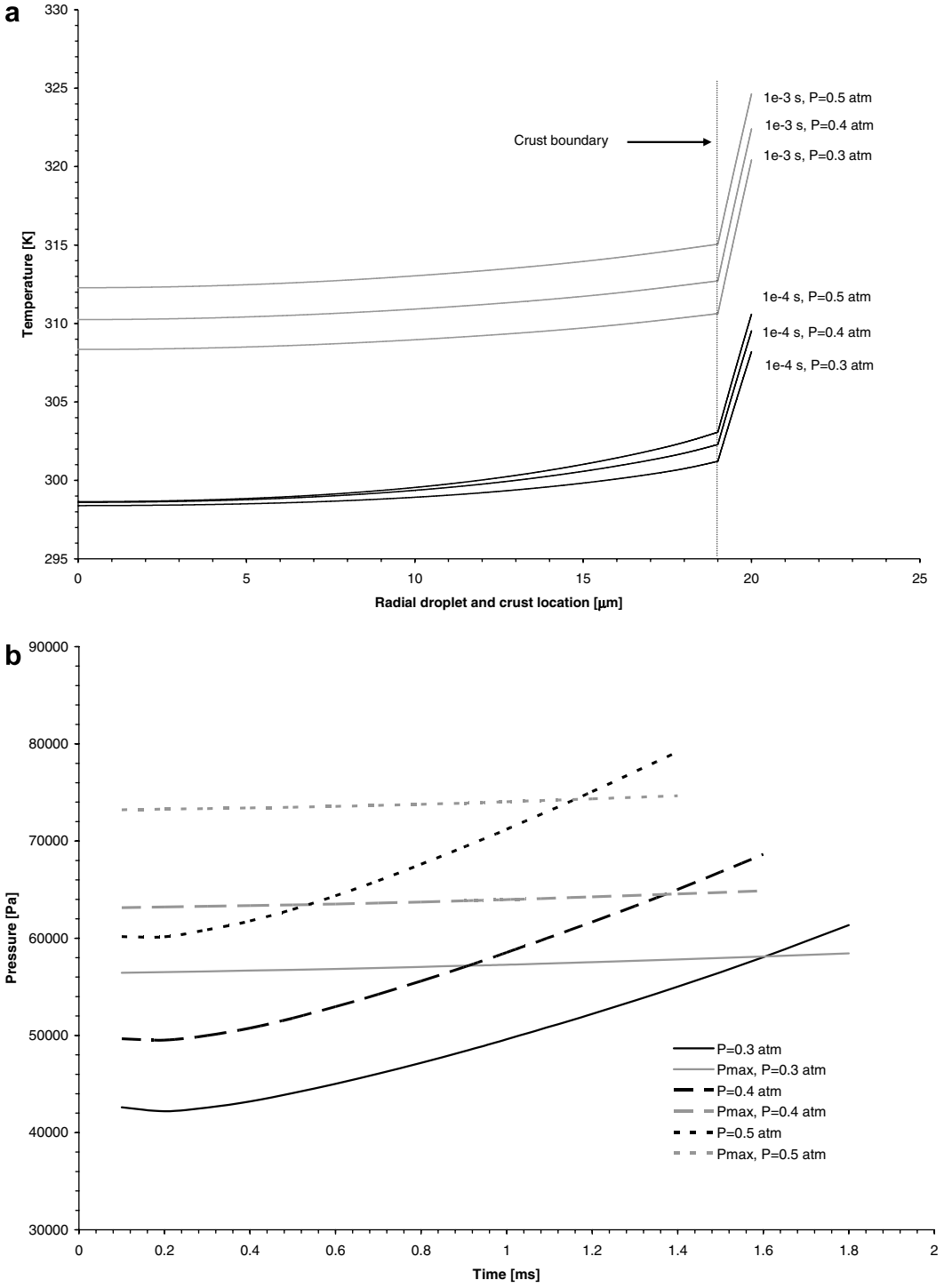


Fig. 9. Temperature profile in the droplet and crust (a) as a function of radial distance and pressure at $1 \times 10^{-4}$ and $1 \times 10^{-3}$ s and evolution of pressure build-up as a function of time (b) for different pressures ($T_\infty = 700$ K for 40 μm diameter droplets, $Z_{Ar} = 0.3/Z_{O_2} = 0.7$, $\varepsilon = 0.5$ and $R_{sp} = 20$ nm).

the droplet and porous crust are presented in Fig. 5a and the salt mass fraction profile in the droplet is shown in Fig. 5b at different times, $1 \times 10^{-4}$ and $1 \times 10^{-3}$ s. There is a sharp temperature gradient across the porous shell in all cases. Higher droplet and porous temperatures are achieved with increasing plasma temperature. The temperature at the centre of the droplet is close to that of the droplet/crust interface. However, the mass fraction profile of salt in the droplet shows a significant difference between those two locations and most changes happen relatively close to the droplet/crust interface. This indicates that heat transfer occurs much faster than mass transfer, suggesting that solvent evaporates and the crust grows inwards increasing its thickness.

The crust/droplet interface recedes faster with increasing temperature as can be seen in Fig. 6a. This phenome-

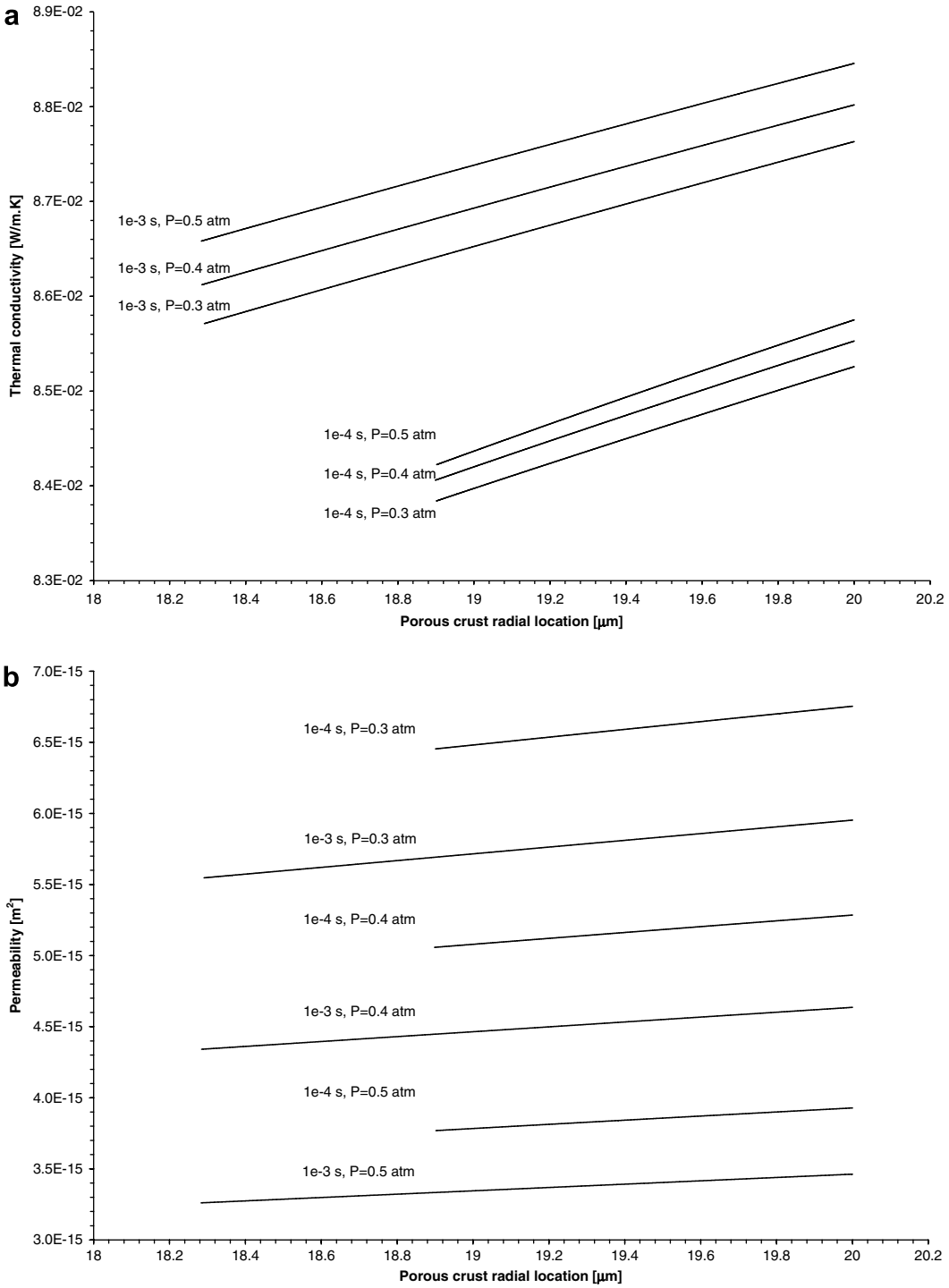


Fig. 10. Thermal conductivity (a) and crust permeability (b) in the porous crust as a function of radial distance at $1 \times 10^{-4}$ and $1 \times 10^{-3}$ s for different pressures ($T_\infty = 700$ K for 40 μm diameter droplets, $Z_{Ar} = 0.3/Z_{O_2} = 0.7$, $\varepsilon = 0.5$ and $R_{sp} = 20$ nm).

non is associated with crust growth and continuing solute precipitation. The pressure at the droplet/crust interface is plotted in Fig. 6b as a function of time. It can be seen that higher heat transfer resulting from increasing plasma temperature causes the pressure inside the droplet to reach the critical "bursting limit" faster. The maximum pressure that the droplet can withstand is independent of the plasma gas temperature, as this pressure largely depends on the amount of solvent contained in the liquid bridges, geometrical considerations and pore size. Solvent surface tension decreases with increasing temperature, but the temperature increase is relatively small and thus surface tension values remain fairly constant at different plasma temperatures.

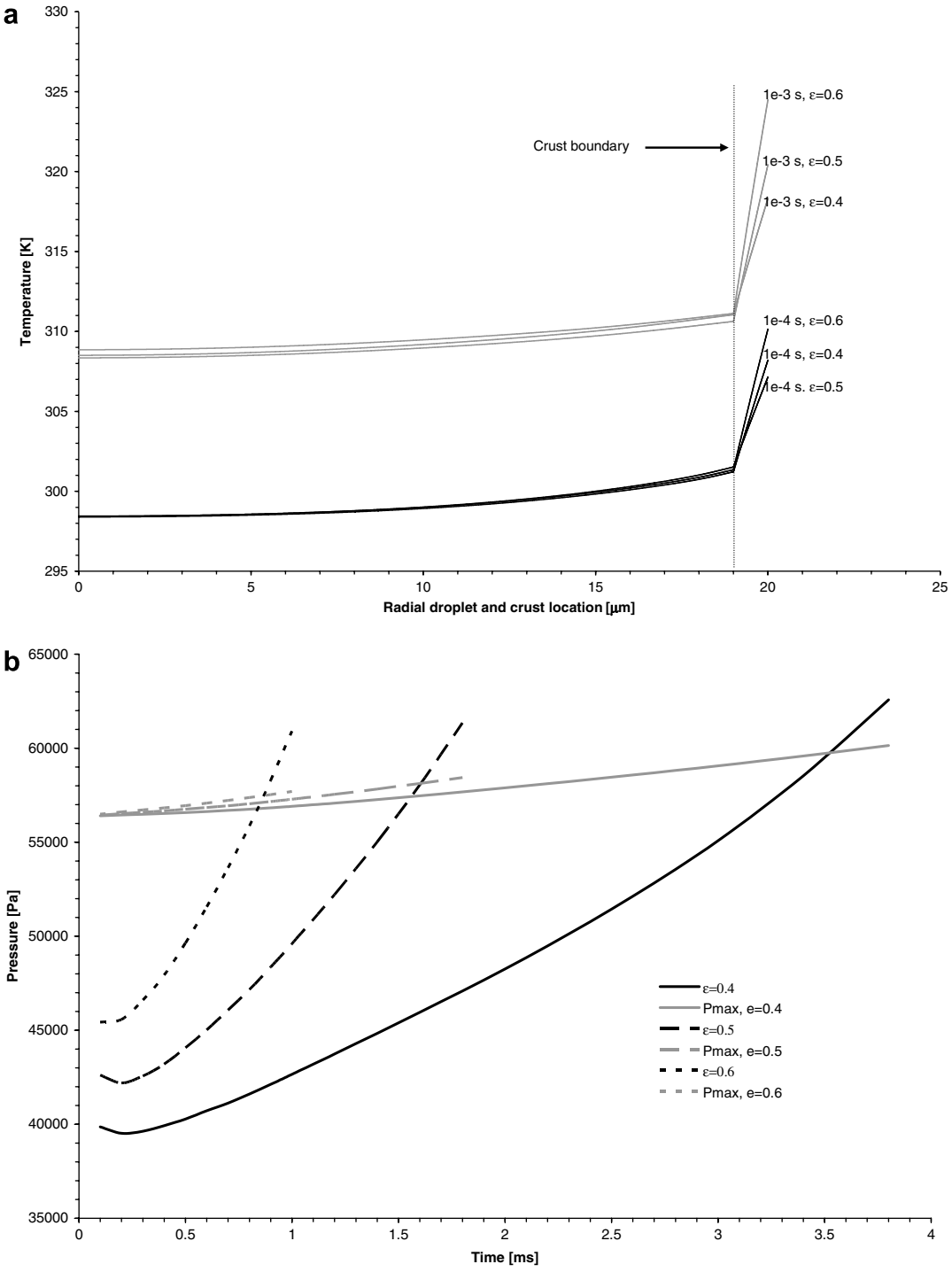


Fig. 11. Temperature profile in the droplet and crust (a) as a function of radial distance and porosity at $1 \times 10^{-4}$ and $1 \times 10^{-3}$ s and evolution of pressure build-up as a function of time (b) for different crust porosities ($P = 0.3$ atm, $T_\infty = 700$ K for 40 μm diameter droplets, $Z_{Ar} = 0.3/Z_{O_2} = 0.7$ and $R_{sp} = 20$ nm).

The apparent pressure decrease seen at the initial stages of Fig. 6b and in some other figures in this work is an artifact of the solution method used to estimate the initial conditions rather than an indication of the physics of the problem. Specifically, this is because the boundary conditions are under-relaxed at the droplet/crust interface, to allow convergence of the solution. This sets the initial pressure slightly higher than originally expected. It must be noted that this erroneous pressure change is very small and is corrected as the solution progresses in time. The important point to notice in this type of figure is the intersection of the pressure lines and the pressure build-up limit lines at the different conditions examined. It may be concluded that the slight initial pressure artifact is only a minor perturbation.

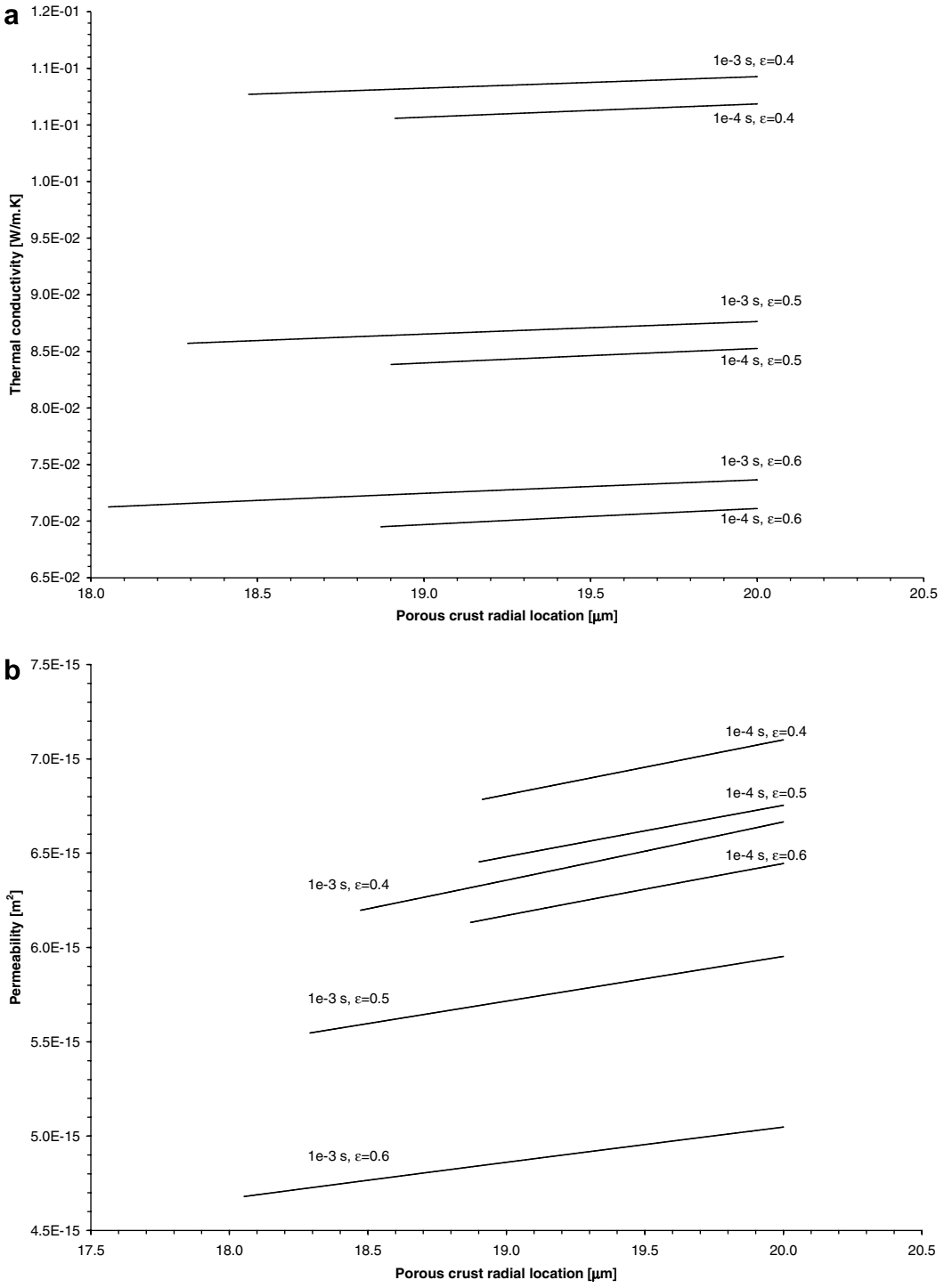


Fig. 12. Thermal conductivity (a) and crust permeability (b) in the porous crust as a function of radial distance at $1 \times 10^{-4}$ and $1 \times 10^{-3}$ s for different porosities ($P = 0.3$ atm, $T_\infty = 700$ K for 40 μm diameter droplets, $Z_{Ar} = 0.3/Z_{O_2} = 0.7$ and $R_{sp} = 20$ nm).

### 4.2. Effect of initial droplet size

The temperature and mass fraction profiles are plotted for different initial droplet diameters (Fig. 7a and b, respectively). It can clearly be observed that the temperature inside the droplet and along the porous crust is higher with smaller droplets. The heat transferred from the surrounding gas to the crust and into the droplet increases as droplets decrease in size due to the higher surface to volume ratio of smaller droplets. Therefore, small droplets are

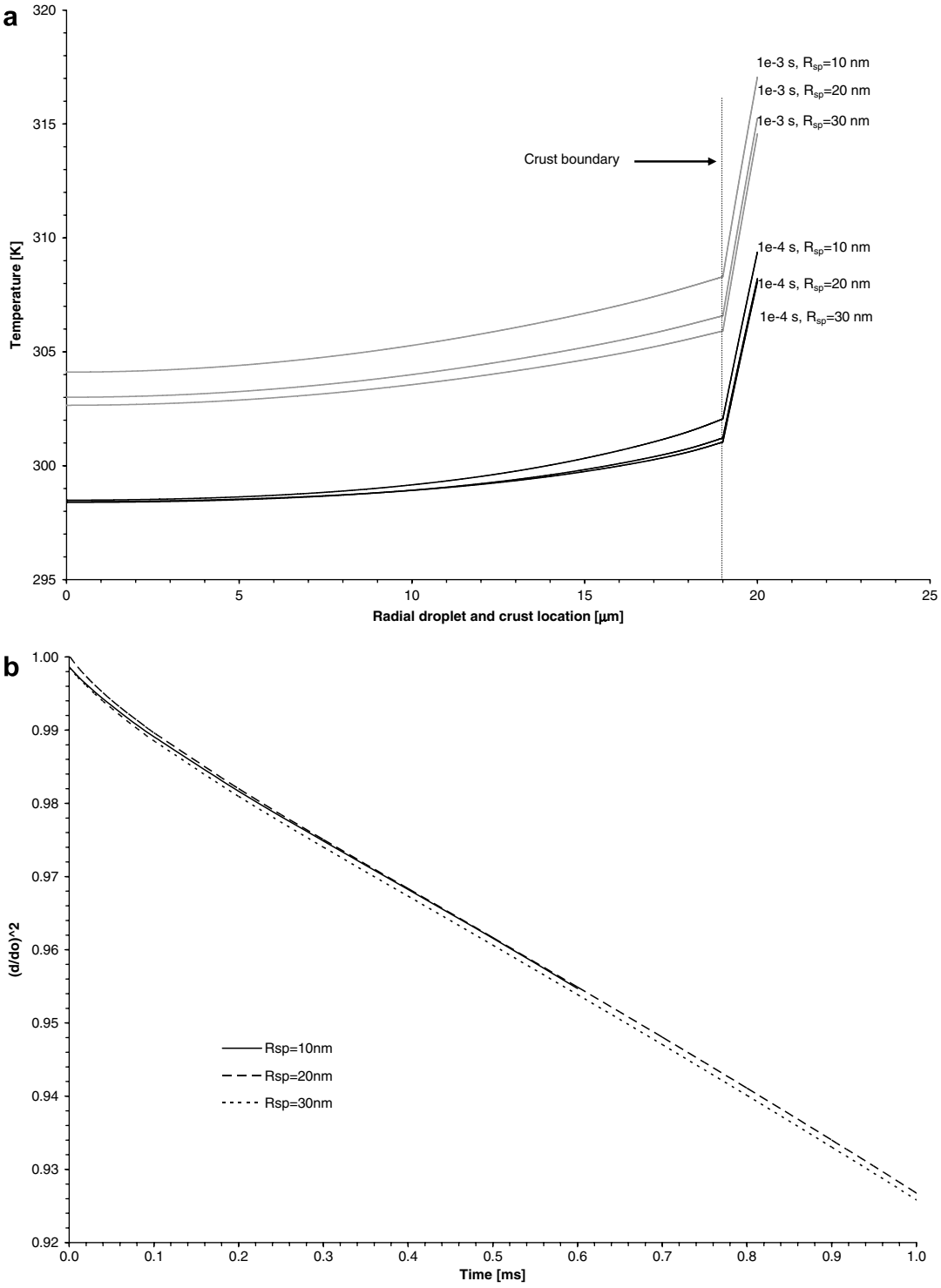


Fig. 13. Temperature profile in the droplet and crust (a) as function of radial distance and size of precipitated crystals at $1 \times 10^{-4}$ and $1 \times 10^{-3}$ s and evolution of droplet diameter (b) for different size crystals ($P = 0.3$ atm, $T_\infty = 700$ K for 40 μm diameter droplets, $Z_{Ar} = 0.3/Z_{O_2} = 0.7$ and $\varepsilon = 0.5$).

heated up faster than larger ones. The rate of mass transfer also increases with decreasing droplet size but once again the mass transfer process is much slower than heat transfer.

As a consequence of the reduced size and higher temperatures, it is expected that smaller droplets will build up pressure at a faster rate. The pressure at the droplet/crust interface is plotted in Fig. 8. This figure shows that smaller droplets reach the critical bursting pressure earlier than large ones. However, smaller droplets also have greater shell strength, as predicted by Eq. (24). The pressure build-up at the droplet core seems to outpace this increasing strength and thus even droplets 30 μm in diameter will burst. The time of droplet bursting is more sensitive to a change in temperature than it is to a change in droplet size (Figs. 6b and 8, respectively). This was calculated by taking the maximum $\Delta T/T$ and $\Delta R_L/R_L$ ratios using the base case as reference and comparing these ratios at the corresponding $\Delta t$. The results indicate that the droplet bursting time is approximately 6 times more sensitive to temperature than it is to droplet size.

### 4.3. Effect of surrounding pressure

The pressure of the plasma gas was changed from 0.3 to 0.5 atm. The temperature profile inside the droplet is plotted at two different times in Fig. 9a. The pressure at the droplet/crust interface as a function of time is shown in Fig. 9b. It can be seen that the temperature in the droplet increases with increasing pressure. The solvent needs a higher temperature to evaporate at the higher system pressure. The droplets subjected to higher pressures tend to burst slightly faster than those at lower pressures (Fig. 9b). The salt mass fraction and droplet shrinkage remain largely unchanged with pressure variations and thus were not plotted.

The fact that higher pressures favor droplet bursting can be further explained by analyzing both the thermal conductivity and crust permeability at different times (Fig. 10a and b, respectively). The crust thermal conductivity is a combination of the conductivity of the gas present in the crust and conductivity of the solid crust material. The solid conductivity is unaffected by pressure but the thermal conductivity of the gas increases with pressure. Also, the crust permeability decreases with increasing pressure. This is a consequence of the Knudsen effect. The mean free path is dependent on pressure, temperature and viscosity. As pressure increases, the viscosity of the gas decreases causing a lowering of the permeability of the crust. Consequently, higher pressures provide slightly higher heat transfer and lower permeability. This favors solvent evaporation and also reduces gaseous solvent flow across the porous crust, hence promoting pressure build-up and crust breakage.

### 4.4. Effect of shell porosity

The crust porosity was varied from $\varepsilon = 0.4$ to 0.6 and temperature and droplet pressure are plotted in Fig. 11a and b, respectively. The droplet temperature remains almost unaltered despite the changing porosity although a steeper temperature gradient is observed for larger poros-

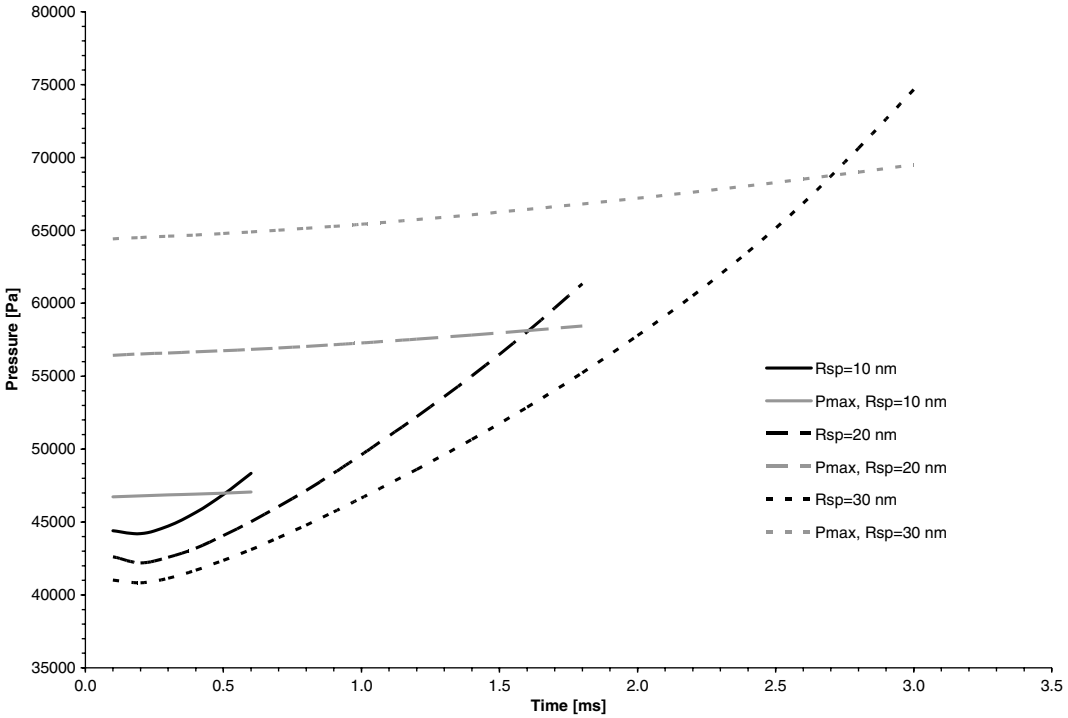


Fig. 14. Evolution of pressure build-up as a function of time for precipitated crystals size ($P = 0.3$, $T_\infty = 700$ K, for 40 μm diameter droplets, $Z_{Ar} = 0.3/Z_{O_2} = 0.7$ and $\varepsilon = 0.5$).

ities. The pressure at the interface is significantly affected by larger porosities (Fig. 11b), and the time taken to reach bursting decreases as the porosity increases.

To further understand these results the thermal conductivity and permeability of the crust are plotted at different times in Fig. 12a and b. The thermal conductivity is appreciably affected by the change in porosity. Higher thermal conductivities are calculated with lower porosity values, because there is more solid material and the conductivity of the solid is higher than that of the gas. The permeability decreases with increasing porosity. This result is counterintuitive but it can be attributed to the Knudsen effect. In this

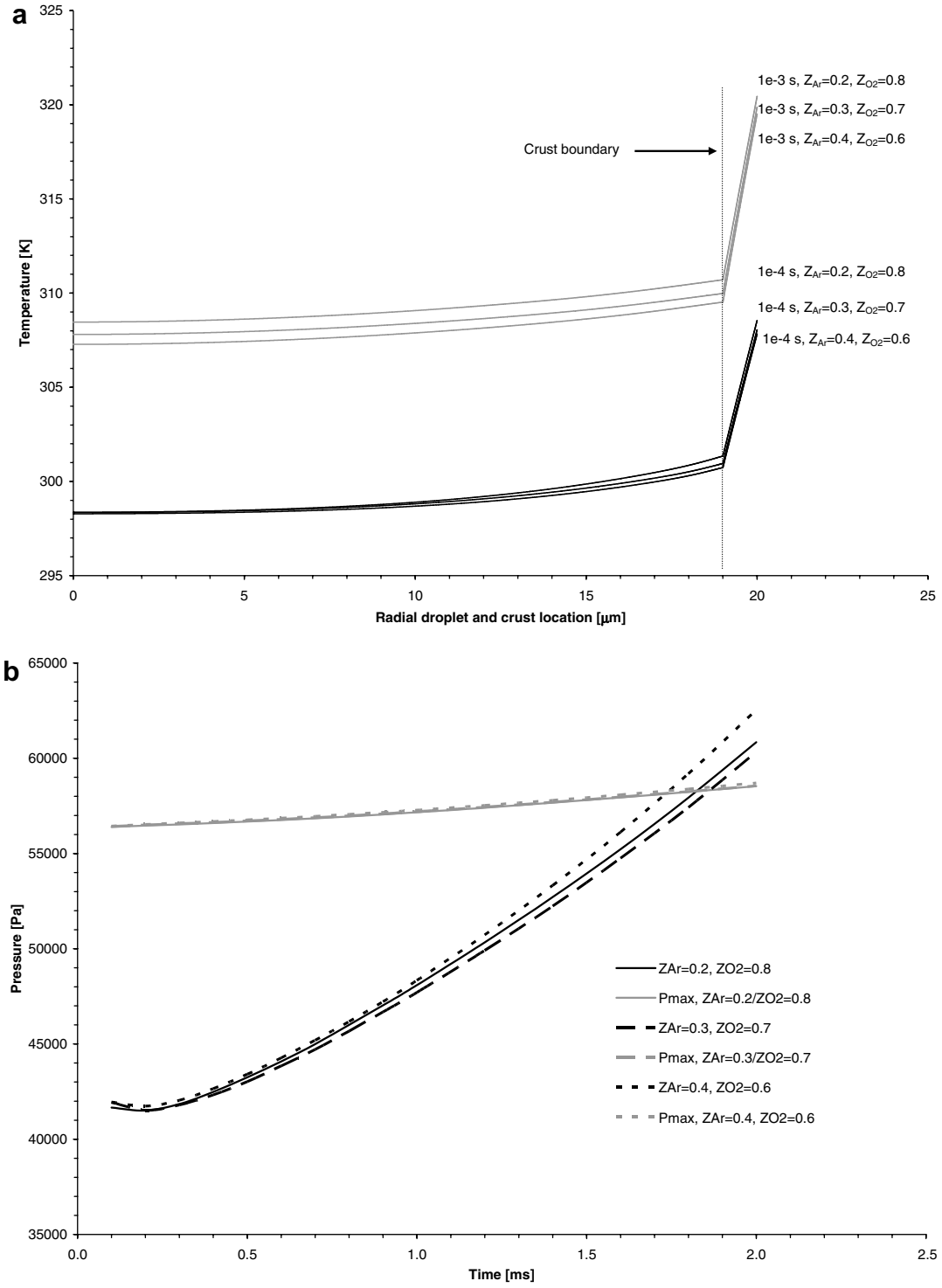


Fig. 15. Temperature profile in the droplet and crust (a) as a function of radial distance and gas composition at $1 \times 10^{-4}$ and $1 \times 10^{-3}$ s and evolution of pressure build-up as a function of time (b) for different gas compositions ($P = 0.3$ atm, $T_\infty = 700$ K for 40 μm diameter droplets, $\varepsilon = 0.5$ and $R_{sp} = 20$ nm).

model, the Knudnsen number lies in the transition regime between continuum and molecular flow. In this regime a change of porosity will not directly affect the permeability of the porous media. The permeability is more dependent on temperature and viscosity rather than on the number of porous channels present in the crust. The smaller porosity directly affects the thermal conductivity which in turn allows more heat to be transferred across the crust. This increases both the temperature and viscosity of the gas. The effect of temperature dominates and thus the permeability increases with decreasing porosity. Finally, as a result of lower permeability crusts, shells of larger porosity tend to break faster as solvent can not escape through the porous media and pressure builds-up.

### 4.5. Effect of size of precipitated crystals in porous crust

The size of the precipitated spherical crystals forming the porous crust was varied from 10 to 30 nm in radius ($10\text{ nm} < R_{sp} < 30\text{ nm}$). The temperature profile inside the droplet was plotted at different times in Fig. 13a and the droplet shrinkage was plotted in Fig. 13b. As the size of the crystals decreases, the temperature inside the droplet increases. This can be explained by higher pressures at the droplet/crust interface which result in a higher solvent evaporation temperature. The pressure increases at the interface because the flow of solvent across the crust meets a larger resistance as a consequence of lower permeability of the crust. In this model the crust pore sizes were assumed to be of the order of the precipitated crystals. The droplet shrinkage seems to remain unchanged despite this slight temperature difference (Fig. 13b) and the salt gradient inside the droplet was also unaffected.

The crust strength on the other hand is greatly affected by the crystal size (Fig. 14). The smaller crystals decrease the pore diameters and allow much less solvent to be present in the liquid bridges formed between crystals. As a result the crust strength is greatly weakened. A simplistic formula was employed in this model to calculate the crust strength as a function of crystal radius (Eq. (24)). The results presented in this model could be refined if a more detailed and accurate model were to be employed but this is beyond the scope of this investigation.

### 4.6. Effect of plasma gas composition

The plasma gas composition was varied by changing the mole fraction of Ar and $O_2$ in the gas $0.6 < Z_{O_2} < 0.8$. The temperature profile inside the droplet and the pressure at the droplet/crust interface were plotted in Fig. 15a and b, respectively. Oxygen rich plasmas have a higher enthalpy than argon rich plasmas at the same temperature, and thus can transfer more heat to the evaporating droplet. As a result, the temperature inside the droplet is slightly higher than for oxygen rich plasmas. The change of plasma gas composition seems to have a limited effect on the strength of porous crust and for all cases the crust burst at very similar exposure times, as shown in Fig. 15b.

## 5. Conclusions

The heat, mass and momentum transfer of an evaporating droplet surrounded by a crust have been solved. Also, a simple model has been developed to understand crust bursting and it has shown that bursting occurs in all cases within the range analyzed. The plasma temperature, initial size of the solution droplet and size of the precipitated spherical crystals played a major role in this process. The effect of crust porosity on crust strength and crust bursting shows that crust permeability is the most important property. This in turn is closely associated with temperature, viscosity and pressure. The Knudsen correction has a large effect on the results obtained because it directly affects the crust permeability. The time for crust rupture lies in the few milliseconds range for all cases from the start of the exposure of the droplet with crust to the plasma gas.

The solvent evaporation and subsequent gaseous flow through the porous crust are largely driven by heat transfer. The flow across the porous crust is dependent on both heat and momentum transfer, whereas mass transfer is considerably slower than the other two processes.

A simple approximation was used to calculate the strength of liquid bridges formed at the crust/droplet interface. However, this approximation proved sufficient to determine a more realistic time of rupture for solution droplets surrounded by porous crusts than previous models reported in the literature.

## Acknowledgements

The financial support by the Natural Sciences and Engineering Research Council of Canada and the Ministry of Education of the Province of Quebec through its FQRNT program is gratefully acknowledged.

## References

[1] E. Bouyer, F. Gitzhofer, M.I. Boulos, Suspension plasma spraying for hydroxyapatite powder preparation by rf plasma, IEEE Trans. Plasma Sci. 25 (5) (1997) 1066–1072.
[2] M. Müller et al., Thermal induction plasma processes for the synthesis of SOFC materials, Materialwiss. Werkst. 33 (6) (2002) 322–330.
[3] E. Bouyer et al., Thermal plasma chemical vapor deposition of Si-based ceramic coatings from liquid precursors, Plasma Chem. Plasma Process. 21 (4) (2001) 523–546.
[4] Delbos et al., DC plasma spray elaboration of fine structured coatings by ceramic liquid suspension injection, in: Proceedings 16th International Symposium on Plasma Chemistry (ISPC 16), Italy, 2003.
[5] Y.C. Lau, P.C. Kong, E. Pfender, Synthesis of zirconia powders in an RF plasma by injection of inorganic liquid precursors, Ceram. Trans. 1 (1988) 298–303.
[6] F. Gitzhofer et al., Integrated fabrication processes for solid-oxide fuel cells using thermal plasma spray technology, MRS Bull. 25 (7) (2000) 38–42.

[7] I. Castillo, R. Munz, Inductively coupled plasma synthesis of $CeO_2$ – based powders from liquid solutions for SOFC electrolytes, Plasma Chem. Plasma Process. 25 (2) (2005) 87–107.
[8] Fauchais, et al, Plasma spraying from thick to thin coatings and micro to nano-structured coatings, in: Proceedings 16th International Symposium on Plasma Chemistry (ISPC 16), Italy, 2003.
[9] L. Jia, F. Gitzhofer, Collection of nano-powders generated by radio frequency (RF) plasma spray synthesis (PSS) processing, using a sampling probe, in: Proceedings 17th International Symposium on Plasma Chemistry (ISPC 17), Canada, 2005.
[10] H. Yu, W.H. Liao, Evaporation of solution droplets in spray pyrolysis, Int. J. Heat Mass Transfer 41 (8–9) (1997) 993–1001.
[11] I. Castillo, R.J. Munz, Transient heat and mass transfer of an evaporating stationary droplet containing dissolved cerium nitrate in a rf thermal argon–oxygen plasma under reduced pressure, Int. J. Heat Mass Transfer 50 (1–2) (2007) 240–256.
[12] D.H. Charlesworth, W.R. Marshall, Evaporation from drops containing dissolved solids, AIChE J. 6 (1) (1960) 9–23.
[13] T. Elperin, B. Krasovitov, Evaporation of liquid droplets containing small solid particles, Int. J. Heat Mass Transfer 38 (12) (1995) 2259–2267.
[14] A. Ozturk, B.M. Cetegen, Modeling of plasma assisted formation of precipitates in zirconium containing liquid precursor droplets, Mater. Sci. Eng. A 384 (2004) 331–351.
[15] D.Y. Byun et al., Microexplosion of aluminum slurry droplets, Int. J. Heat Mass Transfer 42 (1999) 4475–4486.
[16] S.Y. Cho, Some theoretical considerations on the combustion and disruption of free slurry droplets, Combust. Sci. Tech. 67 (1989) 37–57.
[17] F.M. Orr et al., Pendular rings between solids: meniscus properties and capillary force, J. Fluid Mech. 67 (1975) 723.
[18] C. Willett et al., Capillary bridges between two spherical bodies, Langmuir 16 (2000) 9396–9405.
[19] G.H. Tang et al., Gas slippage effect on microscale porous flow using the lattice Boltzmann method, Phys. Rev. E 72 (2005) 056301.
[20] J. Donea et al., Arbitrary Lagrangian Eulerian methods, Encyclopedia of Computational Mechanics, vol. 1, John Wiley and Sons, 2004 (Chapter 14).
[21] Comsol, Comsol multiphysics: modeling guide, Version 3.2 (2005).
[22] W.D. Callister, Materials Science and Engineering: An Introduction, sixth ed., Wiley, 2003.
[23] C.D. Willet et al., Capillary bridges between two spherical bodies, Langmuir 16 (2000) 9396–9405.
[24] Heaviside functions, <http://mathworld.wolfram.com/HeavisdeStepFunction.html>.
[25] H.W. Cheong, A receding interface model for the drying of slurry droplets, AIChE J. 32 (8) (1986) 1334–1346.
[26] Y.S. Touloukian, T. Makita, Thermophysical Properties of Matter: Specific Heat of Non-metallic Liquids and Gases, vol. 6, Plenum, 1970.
[27] J.A. Dean, Lange's Handbook of Chemistry, 15th ed., McGraw Hill, 1999.
[28] R.C. Reid et al., The Properties of Gases and Liquids, fourth ed., McGraw Hill, 1987.
[29] J. Rard et al., Isopiestic determination of the activity coefficients of some aqueous rare earth electrolyte solutions at 25C, J. Chem. Eng. Data 22 (3) (1977).
[30] A. Vasic, A. Cheng, D.C. Groeneveld, A comparison of predictions of high-temperature steam properties, Nuclear Eng. Design 132 (1992) 367–379.
[31] M.I. Boulos, P. Fauchais, E. Pfender, Thermal Plasmas. Fundamentals and Applications, vol. 1, Plenum, 1994.
[32] R.B. Bird, W.E. Stewart, E.N. Lightfoot, Transport Phenomena, second ed., John Wiley & Sons, USA, 2002.
[33] FactSage™, The integrated thermodynamic databank system, Universite de Montreal, Quebec, Canada, 2001.
[34] M. Kaviany, Principles of Heat Transferred in Porous Media, second ed., Springer, USA, 1995.